Reaction
Chemistry &
Engineering

ROYAL SOCIETY
OF CHEMISTRY

PAPER

View Article Online
View Journal | View Issue

Cite this: *React. Chem. Eng.*, 2022, 7, 943

Experimental investigations and model-based optimization of CZZ/H-FER 20 bed compositions for the direct synthesis of DME from CO_2-rich syngas†

Stefan Wild,[a] Bruno Lacerda de Oliveira Campos,[a] Thomas A. Zevaco,[a] David Guse,[b] Matthias Kind,[b] Stephan Pitter,[a] Karla Herrera Delgado*[a] and Jörg Sauer[a]

Received 22nd October 2021,
Accepted 27th December 2021

DOI: 10.1039/d1re00470k

rsc.li/reaction-engineering

Experimental kinetics studies and model-based optimization were performed for the direct synthesis of dimethyl ether (DME) in a wide range of process conditions, including various $CuO/ZnO/ZrO_2$: H-FER 20 bed compositions. Thus, in order to improve the DME productivity using fluctuating CO/CO_2 gas feeds such as those that could be used in power-to-fuel technologies, a series of experiments was carried out at 30 bar by varying the CO_2/CO_x inlet ratio (0.4–0.9), temperature (483–513 K), gas hourly space velocity (2.78, 3.57 s^{-1}), and the weight ratio of the catalyst components $CuO/ZnO/ZrO_2$ and H-FER 20 (from 1 to 70.4). A lumped kinetic model for the methanol synthesis from the literature was extended for the direct DME synthesis. With only eight fitted parameters, the model adequately simulates an extensive array of data points measured with a six-fold parallel reactor setup. The resulting model was applied to optimize the $CuO/ZnO/ZrO_2$: H-FER 20 ratio and the obtained optimization results were validated experimentally, confirming the simulated performance enhancement. For a CO_2-rich feed (CO_2/CO_x = 0.9), the optimum volumetric $CuO/ZnO/ZrO_2$: H-FER 20 ratio under kinetic operating conditions is 91.5/8.5 vol%. Extrapolation based on the new model for industrially relevant operating cases show an optimal H-FER 20 volume fraction below 5 vol%, resulting in a CO_x conversion of 47% at a DME selectivity of 88%.

Introduction

A future with a CO_2-neutral carbon economy necessitates the development of mature power-to-fuel technologies.[1,2] Synthetic fuels and chemicals produced from sustainable and economically viable hydrogen production can compensate for fluctuating and over-potential power generation from renewable energy sources.[3] In addition, adapted synthesis routes can be used to recycle CO_2 yielding CO_2-neutral or even CO_2-consuming fuels and chemicals.[4] One of the most promising options for a flexible and carbon neutral production of chemical energy carriers is the use of CO_2-rich syngas and its further conversion using efficient and long-term stable catalysts. Besides other synthetic hydrocarbons, dimethyl ether (DME) is a particularly interesting product due to its promising physical and chemical properties.[5] DME is the simplest ether, has no C–C bonds and contains oxygen. Therefore, the exhaust gas after the combustion of DME contains less carbon monoxide, unburned hydrocarbons and soot than, for example, during the combustion of butane or diesel.[6] In addition, DME is an attractive intermediate for the chemical industry, *e.g.* for the production of alkyl aromatics, dimethyl sulfate, methyl acetate or light olefins.[7–11]

The industrially applied two-step synthesis requires two individual reactors, one for methanol (MeOH) production, where CO and CO_2 are hydrogenated to MeOH ((R1) and (R2)), linked by the WGS reaction (R3).

CO hydrogenation to MeOH

$$CO + 2H_2 \rightleftharpoons CH_3OH \quad \Delta H°298\ K = -90.4\ kJ\ mol^{-1} \qquad (R1)$$

CO_2 hydrogenation to MeOH

$$CO_2 + 3H_2 \rightleftharpoons CH_3OH + H_2O \quad \Delta H°298\ K = -49.4\ kJ\ mol^{-1} \qquad (R2)$$

Water-gas shift (WGS) and its reverse reaction (rWGS)

---

[a] *IKFT – Institute of Catalysis Research and Technology, Karlsruhe Institute of Technology, Hermann-von-Helmholtz-Platz 1, D-76344 Eggenstein-Leopoldshafen, Germany. E-mail: karla.herrera@kit.edu*

[b] *TVT – Institute of Thermal Process Engineering, Karlsruhe Institute of Technology, Kaiserstraße 12, D-76131 Karlsruhe, Germany*

† Electronic supplementary information (ESI) available. See DOI: 10.1039/d1re00470k

$$CO + H_2O \rightleftharpoons CO_2 + H_2 \quad \Delta H°298\ K = -41.0\ kJ\ mol^{-1} \qquad (R3)$$

In the second reactor, the produced MeOH is consecutively dehydrated to DME (R4).

MeOH dehydration

$$2CH_3OH \rightleftharpoons CH_3OCH_3 + H_2O \quad \Delta H°298\ K = -23.5\ kJ\ mol^{-1} \qquad (R4)$$

The direct DME synthesis with a bifunctional catalyst enables both reactions in one reactor with reduced investment costs. Furthermore, increased CO_x conversion due to the equilibrium shift of reactions (R1) and (R2) is possible.[12–16]

New possible applications of DME in the alternative fuel sectors have not only led to an increase in DME production, but also to numerous research activities in the field of process development[9] to maximize the process efficiency. Particularly for the direct DME synthesis, the effectiveness of the available reactor volume can be improved by optimizing the DME yield as a function of the ratio of MeOH-catalyst/dehydration-agent. The findings, gained through an isochoric optimization of the DME yield, could generally be applied in existing plants with an appropriate reactor concept, without the need for a new reactor design, and thus additional necessary investments. Alternatively, in new plant designs, an optimized catalyst bed ratio enables more compact reactors, thus reducing investment costs. In addition, an optimized catalyst bed composition also represents an opportunity with regard to a possibly improved CO_2 conversion.

The widely studied $CuO/ZnO/Al_2O_3:\gamma\text{-}Al_2O_3$ ($CZA/\gamma\text{-}Al_2O_3$) catalyst system has been investigated in CO-rich syngas from the viewpoint of bed composition (Table 1). For a bed variation of $CZA/\gamma\text{-}Al_2O_3$, Peláez *et al.*[17] reported that the DME yield is increased up to a $CZA/\gamma\text{-}Al_2O_3$ mass ratio of 12.3 (in $H_2/CO = 1.5 - CO_2/CO_x = 0$). Guang-xin *et al.*[18] used a slurry autoclave reactor with a fixed CZA catalyst mass and a successively increasing $\gamma\text{-}Al_2O_3$ mass. They demonstrated that for a pure CO-syngas ($H_2/CO = 1.0 - CO_2/CO_x = 0$), the maximum CO conversion is found at a $CZA:\gamma\text{-}Al_2O_3$ weight ratio of 20. A further mass increase of $\gamma\text{-}Al_2O_3$ leads to a decrease in CO conversion. The DME selectivity reaches a nearly constant value at a $CZA/\gamma\text{-}Al_2O_3$ mass ratio of 8, whereas a minor loading of $\gamma\text{-}Al_2O_3$ showed a significant decrease in DME selectivity.

A catalyst bed variation using CO_2-rich syngas was studied by Peinado *et al.*[19] with $CZA/\gamma\text{-}Al_2O_3$ ($CO/CO_2/H_2$: 1/1.9/7.7 – $CO_2/CO_x = 0.66$) showing increased CO_x conversions (up to 24 mol%) for a $CZA/\gamma\text{-}Al_2O_3$ weight ratio of 9. However, DME was only converted from CO_x with a selectivity of 1%. Increasing the amount of $\gamma\text{-}Al_2O_3$ in the bed improved the DME selectivity, but at the expense of CO_x conversion. Bae *et al.*[20] also investigated a bed variation of the $CZA/\gamma\text{-}Al_2O_3$ catalyst system for a CO/CO_2 syngas mixture of $CO/CO_2/H_2$: 41/21/38 – $CO_2/CO_x = 0.34$. Here, CO conversion (29.3 mol%) is increasing up to a $CZA:\gamma\text{-}Al_2O_3$ weight ratio of 5, however, accompanied by a decrease in DME selectivity (7.9 mol%). In a recent study, Delgado Otalvaro *et al.*[21] found similar results with a variable CO_2/CO_x feed, where an increasing $CZA/\gamma\text{-}Al_2O_3$ ratio promotes CO_x conversion and a DME yield at a low CO_2 content in the feed; however, a high CO_2 feed content significantly reduces DME selectivity.

Catalyst systems involving zeolites (Table 1) as dehydrating agents have also been investigated for CO-rich syngas compositions. Abu-Dahrieh *et al.*[22] investigated a combination of CZA/HZSM-5 (Si/Al = 80) and found an increased DME yield for a CZA:HZSM-5 mass ratio of 3 at 533 K, 20 bar ($H_2/CO/CO_2/Ar$: 62/31/4/3 – $CO_2/CO_x = 0.11$). García-Trenco *et al.*[23] investigated a variation of a hybrid catalyst system consisting of CZA/H-ZSM-5 (Si/Al = 40) under similar conditions ($H_2/CO/CO_2$: 66/30/4 – $CO_2/CO_x = 0.12$, 40 bar and 533 K) and found that even at a CZA:H-ZSM-5 mass ratio of 9, no significant decrease in the DME yield takes place.

A catalyst bed variation of H-ZSM5 in combination with a fixed CZA catalyst mass[24] in a pure CO_2 syngas feed ($CO_2/CO_x = 1.0$) revealed a nearly stable CO_2 conversion (26 mol%) while DME selectivity remained constant up to a CZA:HZSM-5 mass ratio of 5.

Arena *et al.*[26] reported the advantages of CZZ compared to CZA systems in the scope of CO_2 hydrogenation. Extensive studies of a $CuO/ZnO/ZrO_2$:H-FER 20 (CZZ/FER) catalyst system revealed that the catalyst system showed promising activity for flexible conversion of both CO-rich and CO_2-rich syngas to DME, as well as superior activity compared to a commercial CZA system,[27,28] confirming the aforementioned

Table 1 A literature summary of optimal catalyst bed compositions in the direct DME synthesis

MeOH catalyst	Dehydr. catalyst	Optimal[a,b] MeOH/Dehydr. catalyst mass ratio	CO_2/CO_x	Ref.
CZA	$\gamma\text{-}Al_2O_3$	12.3[a]	0.0	Peláez *et al.*[17]
CZA	$\gamma\text{-}Al_2O_3$	20[b]	0.0	Jia *et al.*[25]
CZA	$\gamma\text{-}Al_2O_3$	9[b]	0.66	Peinado *et al.*[19]
CZA	$\gamma\text{-}Al_2O_3$	5[b]	0.34	Bae *et al.*[20]
CZA	$\gamma\text{-}Al_2O_3$	2[b]	0.2/0.4/0.6/0.8	Delgado Otalvaro *et al.*[21]
CZA	H-ZSM-5	9[a]	0.12	García-Trenco *et al.*[23]
CZA	H-ZSM-5	5[a]	1.0	Ren *et al.*[24]

[a] Based on DME yields. [b] Based on CO_x conversion.

favorable activity of Zr-promoted Cu/ZnO systems in CO_2-rich environments. A comparison of the dehydration properties of γ-Al_2O_3 and FER at different CO_2/CO_x syngas ratios shows that DME selectivity is less affected for both in CO-rich and CO_2-rich syngas when FER is used,[27,29] suggesting that even at higher CZZ ratios, better CO_x conversion and thus higher DME yields are possible. Based on the current state of knowledge, a detailed understanding of the dependency of the process variable conversion and selectivity at large CZZ/FER ratios is of great interest. Besides, the dependence on the syngas composition is important as both CO and CO_2 can be converted[27] and the transition from WGS (R3) to the rWGS reaction is observable to reveal the respective correlations between the catalyst bed composition and CO/CO_2 hydrogenation ((R1) and (R2)).

To the best of our knowledge, such a broad range of operating conditions has not been studied or modeled yet. Our hypothesis is that important impulses for further process development will be derived from the knowledge of syngas composition dependencies. Herein, we investigate the catalyst bed composition of the system CZZ/FER at different process parameters, *i.e.* the CO_2 content in the synthesis gas, temperature and space time. To describe and simulate a wide operating range, a kinetic model was developed to calculate an optimized CZZ/FER ratio within the studied operating conditions. The model is also applied for predicting the process performance at industrially relevant operating cases.

For CO_2 hydrogenation to DME, Ren *et al.*[24] showed that the mixing method of the catalyst components (CZA/HZSM-5) has a minor impact on conversion and the DME yield but significantly influences catalyst stability. Similarly, in a CO-rich environment as reported by García-Trenco *et al.*,[23] slightly increased conversion is observed with a physically mixed bed compared to a hybrid mixed bed configuration. It has also been reported[30,31] that due to closer contact within a hybrid catalyst, Cu and even Zn ion migration from the MeOH-forming catalyst into the dehydration component may occur, reducing both acidity and the available Cu and Cu/Zn surface areas. Also, increased Cu migration into the zeolite pores was found by Fierro *et al.*[32] at elevated water vapour concentrations. Accordingly, a higher CO_2 feed content should increase Cu migration due to enhanced water production *via* the rWGS reaction (R3). In order to reduce these transport effects, the catalytic components used in this work were separately pressed, sieved and subsequently physically mixed, as described afterwards.

Experimental

Catalyst preparation

The CZZ catalyst was prepared by a continuous co-precipitation method from metal nitrate and sodium bicarbonate solutions resulting in pH 7 using a micro jet mixer.[28] The suspension was then aged at 313 K for 2 h. The solids were filtered, dried at 383 K for 16 h and calcined at 623 K with 3 K min^{-1} for 4 h. Characterization techniques used were described in a previous work.[28] A commercial ferrierite-type zeolite H-FER 20 (FER) from Zeolyst International with a Si/Al ratio of 20 was used as a dehydration catalyst. Before use, FER was calcined at 823 K for 4 h in air.

Catalyst characterization

Selected chemical and physical data of the CZZ catalyst are shown in Table 4. The XRD analysis of the CZZ catalyst precursor and the calcined pre-catalyst can be found in chapter S9.† Physico-chemical properties of FER are taken from a study by Kim *et al.*[33] and shown in Table 5.

Catalytic activity study

Each catalyst component was finely powdered, pressed and sieved into fractions of 250–500 μm, followed by physical mixing of the components in the required mass ratio. The studied catalytic bed configurations are summarized in Table 2. Within this sieve fraction, the bulk density amounts to 882.5 kg m^{-3} for CZZ and to 415.0 kg m^{-3} for FER.

The catalyst beds were 100 ± 1 mm in length. The physical mixtures were diluted with silicon carbide (SiC, Hausen Mineraliengroßhandel GmbH) of the same grain size as the catalyst components for isothermal operation. To ensure an adequate grain distribution of the catalytic components CZZ, FER and SiC, the beds were filled as five-fold stacks. The catalyst bed volume was constant at 4.20 ml. At the top and bottom of the beds, additional SiC layers were placed.

Direct DME synthesis was performed in a self-constructed parallel reactor system "MURSS" (multi-reactor-screening-system, see Fig. 1 and S2†) with stainless steel fixed bed reactors (inner diameter: 17.4 mm; length: 600 mm). Each reactor can be independently heated with heating cartridges and brass jaws over a length of 400 mm. A catalyst bed temperature profile is measured using axial thermocouples. Gas supply is controlled using mass flow controllers (Bronkhorst Hi-Tec). Feed gases, carbon monoxide (CO, 99.97 vol%), nitrogen (N_2, 99.9999 vol%), hydrogen (H_2, 99.9999 vol%) and a mixture carbon of CO_2/N_2 ($50:50 \pm 1.0$ vol%), were supplied by Air Liquid Germany GmbH. The total inlet gas flow is distributed *via* a capillary system, with fine flow adjustment by flow meters before each reactor. A volume fraction of approx. 5 vol% of the reactor outlet gas flows and the bypass flow is directed to a multi-position valve (Valco), which is connected to a FTIR CX4000 (Gasmet Technologies Oy) equipped with a micro gas chromatograph (Inficon Micro

Table 2 Catalyst bed (CB) compositions of CZZ/FER

Catalyst bed no. [—]	CZZ [wt%]	FER [wt%]	CZZ [vol%]	FER [vol%]
CB 1	50.0	50.0	32.0	68.0
CB 2	81.2	18.8	67.0	33.0
CB 3	89.5	10.5	80.0	20.0
CB 4	95.0	5.0	90.0	10.0
CB 5	98.6	1.4	97.0	3.0

Table 3 CO_2/CO_x inlet ratios and respective feed gas compositions used in the direct DME synthesis

CO_2/CO_x	CO/vol%	CO_2/vol%
0.40	12.0	8.0
0.60	8.0	12.0
0.70	6.0	14.0
0.75	5.0	15.0
0.80	4.0	16.0
0.90	2.0	18.0

GC Fusion). The GC is equipped with two thermal conductivity (TCD) detectors connected to RT-Molsieve 5A, 0.25 mm (10 m) and RT-Q-Bond, 0.25 mm (12 m) columns. Each operating point was held for 200 min and the catalyst beds were measured consecutively. After finishing the variation loops of CO_2/CO_x values for each temperature, the reactor was purged with N_2 for one hour (the general sequence of the process parameters is shown in Fig. S1†).

Reduction of the CZZ catalyst volume fraction was performed at 2 bar with 5 vol% H_2 diluted in N_2, while temperature was increased from 373 K to 473 K with a ramp of 10 K h^{-1}, followed by further heating to a final reduction temperature of 493 K with 50/50 vol% H_2/N_2 at a rate of 10 K h^{-1}. After another 60 min, the reactor was purged with N_2, cooled to 483 K and, subsequently the pressure increased to 30 bar. The feed gas composition was $H_2/CO_x/N_2$ = 45/20/35 vol%, and the considered CO and CO_2 feed concentrations respectively CO_2/CO_x inlet ratios are shown in Table 3. Before kinetic measurements, the catalyst beds were exposed to a run-in period of 75 h time on stream (ToS) by varying the temperature (493, 503, and 513 K), CO_2/CO_x inlet ratio (0.4, 0.7, and 0.9) and gas hourly space velocity (GHSV) (2.78 and 3.57 s^{-1}) at 30 bar. These measurements were used for the validation of the optimized catalyst bed ratio. The kinetic measurements were performed at each feed gas composition shown in Table 3, with temperatures between 483 and 513 K and two GHSV values of 2.78 and 3.57 s^{-1} with regard to the catalyst volume.

Experimental error analysis

Before starting the kinetic investigations, the experimental error of the novel system (Fig. 1) was estimated to verify that the data quality in parallel operation is in a similar range to when using a single PFR system. The error caused by an unequal flow distribution *via* the capillary system is in the range of ±1.2–1.5%. The complete error analysis and the error estimation can be found in S3.†

Performance indicators

In all experiments, the carbon balance (eqn (S1)†) presented a maximum deviation of ±3%. The CO_x conversion is calculated as follows (eqn (1)):

$$X_{CO_x} = \frac{\dot{n}_{CO,in} - \dot{n}_{CO,out} + \dot{n}_{CO_2,in} - \dot{n}_{CO_2,out}}{\dot{n}_{CO,in} + \dot{n}_{CO_2,in}} \tag{1}$$

where $\dot{n}_i$ is the respective molar flowrate. The role (*i.e.* reactant or product) of CO and CO_2 on DME and MeOH formation is represented by the CO and CO_2 conversion (eqn (2) and (3)):

$$X_{CO} = \frac{\dot{n}_{CO,in} - \dot{n}_{CO,out}}{\dot{n}_{CO,in}} \tag{2}$$

$$X_{CO_2} = \frac{\dot{n}_{CO_2,in} - \dot{n}_{CO_2,out}}{\dot{n}_{CO_2,in}} \tag{3}$$

The oxygenate/hydrocarbon-based selectivity (eqn (4)) is used to obtain a selectivity independent of the possibly produced CO_2 and CO:

$$S_{C_xO_yH_z,CO_2+CO} = \frac{v_x \dot{n}_{C_xO_yH_z}}{\sum v_x \dot{n}_{C_xO_yH_z}} \tag{4}$$

Here, v_x corresponds to the number of carbon atoms in each $C_xO_yH_z$ product. Formation of DME and MeOH with respect to each catalyst bed is calculated as volumetric DME and MeOH productivities (eqn (5) and (6)):

$$P_{DME,V_{bed}} = \frac{\dot{m}_{DME,out}}{V_{cat\text{-}bed}} \left[g_{DME}\ L_{cat\text{-}bed}{}^{-1}\ h^{-1} \right] \tag{5}$$

$$P_{MeOH,V_{bed}} = \frac{\dot{m}_{MeOH,out}}{V_{cat\text{-}bed}} \left[g_{MeOH}\ L_{cat\text{-}bed}{}^{-1}\ h^{-1} \right] \tag{6}$$

Kinetic model development

Kinetic description of the direct DME synthesis is based on the six-parameter model for the MeOH synthesis from Lacerda de Oliveira Campos *et al.*,[34] which has been extended to include the MeOH dehydration step.

In the MeOH synthesis model, only CO_2 hydrogenation (eqn (7)) and the rWGS reaction (eqn (8)) are considered, as theoretical studies suggest that direct CO hydrogenation is not significant at a moderate or high CO_2 content.[35,36] The reaction rates of CO_2 hydrogenation (r_{CO_2} mol s^{-1}) and rWGS (r_{rWGS} mol s^{-1}) are shown as follows:

Table 4 Selected properties of the CZZ catalyst component

Catalyst	Cu/wt%	Zn/wt%	Zr/wt%	$S_{BET}/m^2\ g^{-1}$	$S_{Cu}/m^2\ g^{-1}$	d_{CuO}/nm calcined catalyst
CZZ	62	31	7	98	36	7

d_{CuO}: CuO crystallite size (XRD). S_{Cu}: specific copper surface area (N_2O-RFC). S_{BET}: Brunauer–Emmett–Teller (BET) surface area.

Table 5 BET surface areas and total acidity properties of the acid dehydration catalyst FER at low-temperature (LT) and high-temperature (HT) taken from the study by Kim *et al.*[33]

		NH_3-TPD peak positon/K		Acid amount/mmol NH_3 per g_{cat}		
Catalyst	S_{BET}/$m^2\ g^{-1}$	LT region	HT region	Total acidity	LT region	HT region
FER	390	481	656	0.70	0.31	0.39

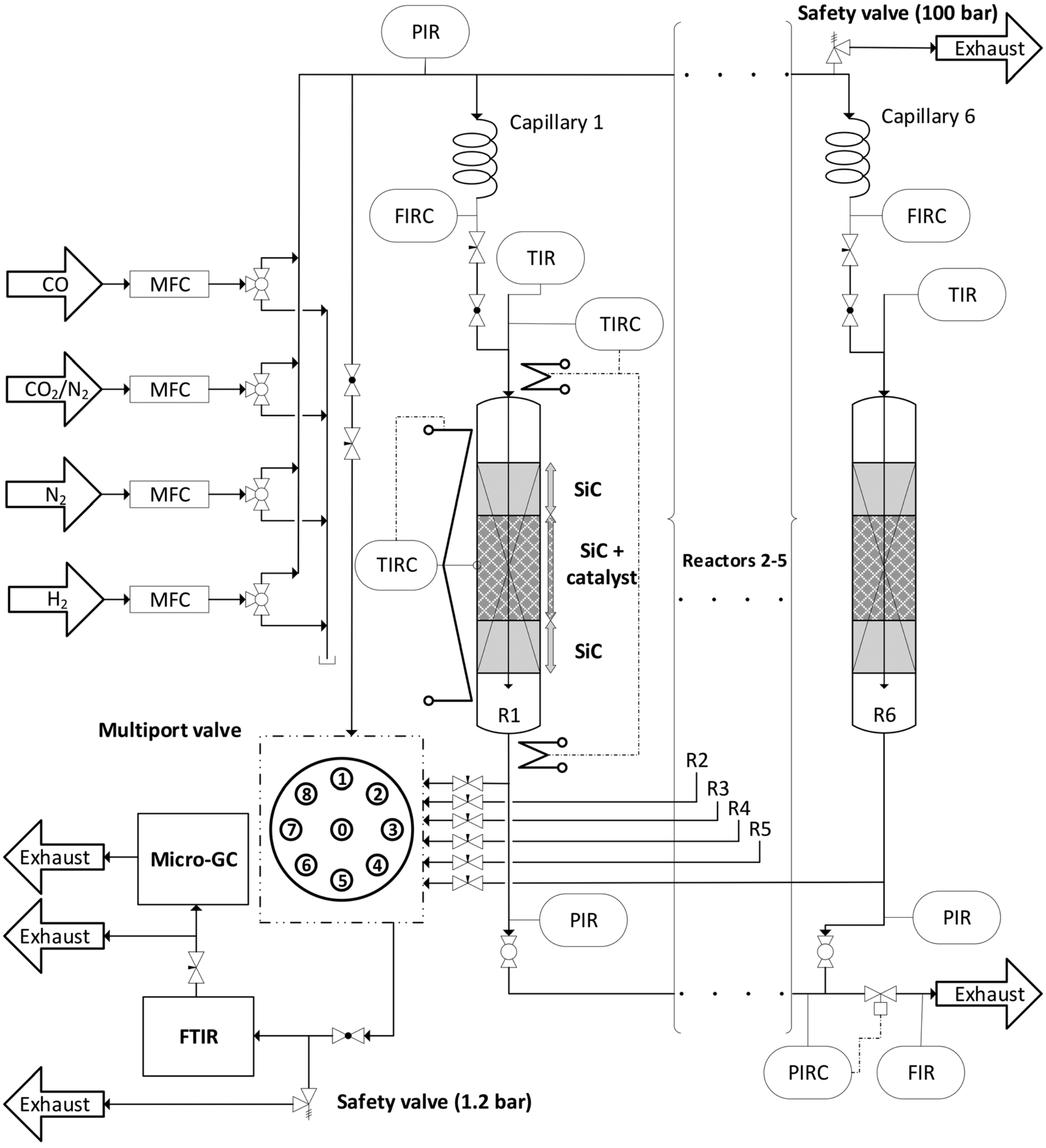

Fig. 1 A schematic flow chart of the parallel reactor system.

$$r_{CO_2hyd} = m_{CZZ}\cdot \exp\left(k_{0,CO_2hyd} - \frac{E_{A,CO_2hyd}}{R\cdot T}\right)\cdot \phi_{Zn}\cdot\theta_b\cdot\theta_c\cdot f_{H_2}{}^{1.5} \cdot f_{CO_2}\cdot\left(1 - \frac{f_{CH_3OH}\cdot f_{H_2O}}{f_{H_2}{}^{3}\cdot f_{CO_2}\cdot K_{P,CO_2hyd.}{}^{0}}\right) \quad (7)$$

$$r_{rWGS} = m_{CZZ}\cdot \exp\left(k_{0,rWGS} - \frac{E_{A,rWGS}}{R\cdot T}\right)\cdot \phi_{Zn}\cdot\theta_b\cdot\theta_c\cdot f_{CO_2}\cdot f_{H_2O} \cdot\left(1 - \frac{f_{CO}\cdot f_{H_2O}}{f_{CO_2}\cdot f_{H_2}\cdot K_{P,rWGS}{}^{0}}\right) \quad (8)$$

where m_{CZZ} is the mass of the CZZ catalyst (kg), k_{0,CO_2hyd} and $k_{0,rWGS}$ are the reaction rate constants, E_{A,CO_2hyd} and $E_{A,rWGS}$ are the activation energies, ϕ_{Zn} is the zinc coverage on the catalyst surface, θ_b is the coverage of free Cu/Zn sites, θ_c is the coverage of free sites available only for H_2 and H_2O, f_j is the fugacity of gas component j (bar), and $K_{P,CO_2hyd.}{}^0$ (bar^{-2}) and $K_{P,rWGS}{}^0$ are the global equilibrium constants. The zinc coverage varies depending on the gas composition.[37,38] We investigated theoretical approaches for the zinc coverage estimation (Kuld *et al.*[38] and Ovesen *et al.*[39]), but the additional zinc coverage estimation did not improve the simulation results. Still, in our operating region of interest (CO_2/CO_x between 0.40 and 0.90), we assumed that the zinc coverage change is small enough for a simplified constant value to be considered. Therefore, we followed the approach of Lacerda de Oliveira Campos *et al.*[34] of considering a constant zinc coverage value of 0.50.

The fugacity coefficients are calculated with the Peng–Robinson equation, using binary interaction parameters and other parameters from the literature.[40,41] The free sites θ_b and θ_c are calculated as follows:

$$\theta_b = \left(\frac{1}{1 + K_1\cdot f_{CO_2}\cdot f_{H_2}{}^{0.5}}\right) \tag{9}$$

$$\theta_c = \left(\frac{1}{1 + K_2\cdot f_{H_2O}\cdot f_{H_2}{}^{-0.5}}\right) \tag{10}$$

Here, K_1 (bar$^{-1.5}$) and K_2 (bar$^{-0.5}$) are the adsorption constants. Arvidsson *et al.*[42] performed density functional theory (DFT) calculations for MeOH dehydration on different zeolites and found that the associative mechanism is dominant at temperatures lower than 573 K. In our work, we assume that the reaction mechanism of MeOH dehydration over FER is also the associative path. This mechanism consists of two elementary reactions: the MeOH adsorption (eqn (11)) and the associative reaction (eqn (12)),

$$\text{Z–H} + CH_3OH_{(g)} \rightleftarrows \text{Z–H–}CH_3OH \tag{11}$$

$$\text{Z–H–}CH_3OH + CH_3OH_{(g)} \rightleftarrows CH_3OCH_{3(g)} + H_2O_{(g)} + \text{Z–H} \tag{12}$$

where Z–H is a free acid site and Z–H–CH$_3$OH represents the adsorbed MeOH. Considering the associative reaction (eqn (12)) as the rate determining step (RDS),[42] the reaction rate of MeOH dehydration (r_{Dehyd}, mol s^{-1}) is calculated in eqn (13). The mathematical derivation of this reaction rate is provided in the ESI.†

$$r_{Dehyd} = m_{FER}\cdot \exp\left(k_{0,Dehyd} - \frac{E_{A,Dehyd}}{R\cdot T}\right)\cdot\theta_d\cdot f_{MeOH}{}^2 \cdot\left(1 - \frac{f_{DME}\cdot f_{H_2O}}{f_{MeOH}{}^2\cdot K_{P,Dehyd}{}^0}\right) \tag{13}$$

Here, m_{FER} is the mass of FER (kg), k_{Dehyd} is the MeOH dehydration rate constant, θ_d is the coverage of free zeolite sites, and $K_{P,Dehyd}{}^0$ is the global equilibrium constant. It should be noted that the rate of MeOH dehydration over FER can be affected by mass transfer limitations, due to the microporous nature of the zeolites. However, in this model, we assume that there are no significant mass transfer limitations, due to the small particle size range of FER (250–500 μm). The coverage of the free zeolite sites (θ_d) is calculated as follows:

$$\theta_d = \left(\frac{1}{1 + K_3\cdot f_{MeOH}}\right) \tag{14}$$

where K_3 (bar^{-1}) is an adsorption constant. The kinetic model has initially nine parameters to be estimated: the reaction rate constants (k_{0,CO_2hyd}, $k_{0,rWGS}$, and $k_{0,Dehyd}$), the activation energies (E_{A,CO_2hyd}, $E_{A,rWGS}$, and $E_{A,Dehyd}$), and the adsorption constants (K_1, K_2, and K_3). Using our experimental database, it was found that $E_{A,Dehyd}$ is statistically not significant, probably because the MeOH dehydration is at quasi-equilibrium for operating points with high amounts of FER. Therefore, $E_{A,Dehyd}$ is excluded from the model ($E_{A,Dehyd} = 0$) and eight remaining parameters (k_{0,CO_2hyd}, $k_{0,rWGS}$, $k_{0,Dehyd}$, E_{A,CO_2hyd}, $E_{A,rWGS}$, K_1, K_2, and K_3) are to be estimated.

The estimation of the kinetic parameters is done by solving an optimization problem, where the objective function is the minimization of the normalized squared errors of the prediction ($\hat{y}^i_{out,j}$) of the carbonaceous compounds (CO, CO$_2$, MeOH and DME), the so-called chi-squared (χ^2) regression method. The normalization with experimental $y^i_{out,i}$ squared values is performed to prevent overweighting of high conversion points and underweighting of low conversion points.

$$\chi^2 = \sum_{i=1}^{N_p}\left[\frac{\left(y^i_{out,CO} - \hat{y}^i_{out,CO}\right)^2}{\left(y^i_{out,CO}\right)^2} + \frac{\left(y^i_{out,CO_2} - \hat{y}^i_{out,CO_2}\right)^2}{\left(y^i_{out,CO_2}\right)^2} + \frac{\left(y^i_{out,MeOH} - \hat{y}^i_{out,MeOH}\right)^2}{\left(y^i_{out,MeOH}\right)^2} + \frac{\left(y^i_{out,DME} - \hat{y}^i_{out,DME}\right)^2}{\left(y^i_{out,DME}\right)^2}\right] \tag{15}$$

Here, N_p is the number of data points in the training set, $y^i_{out,j}$ is the experimental output mole fraction of gaseous component j at the operating point i, and $\hat{y}^i_{out,j}$ is the simulated output mole fraction of gaseous component j of the operating point i.

Table 6 Fitted parameters of $k_{0,i}$, $E_{a,i}$ and K_i within the training set

	k_{0,CO_2} [—]	$k_{0,rWGS}$ [—]	$k_{0,DME}$ [—]	E_{A,CO_2} kJ mol^{-1}	$E_{A,rWGS}$ kJ mol^{-1}	K_1 Bar$^{-1.5}$	K_2 Bar$^{-0.5}$	K_3 Bar^{-1}
Best-fit	9.57	26.23	3.08	75.53	119.71	0.38	8.28	52.92
CI±	0.44	2.43	0.54	2.29	9.44	0.14	0.90	30.14

In order to figure out the best parameter set and to calculate the confidence intervals, a 5-fold cross validation (CV) method was used.[43,44] The 240 experimental points were randomly divided into five groups of 48 points each, and the optimization problem was solved five times, each one with four of the five groups as a training set, resulting in five sets of parameters. The group of parameters with which the model has the lowest χ^2 value for the total 240 points is chosen as the best one. The confidence interval (CI) of each parameter is derived by calculating the standard deviation of each parameter considering the five parameter sets and multiplying by the *t*-student factor (0.05 two-tail significance and 232 degrees of freedom). The optimization problems are solved with the Matlab function fminsearch (varying the starting values).

The 5-fold cross validation ($CV_{(5)}$) value is a mean value of the χ^2 five different parameter sets (eqn (16)). The closer it is to the χ^2 value of the best fit, the better the model should simulate experiments outside the training set.

$$CV_{(5)} = \sum_{i=1}^{5} {\chi_i}^2 \tag{16}$$

The mean squared error (MSE) and the mean error (ME) are also statistical indicators of the model quality. They are calculated for each component *j* according to eqn (17) and (18).

$$MSE_j = \sum_{i=1}^{N_p} \frac{\left(y^i_{out,j} - \hat{y}^i_{out,j}\right)^2}{\left(y^i_{out,j}\right)^2} \tag{17}$$

$$ME_j = \sum_{i=1}^{N_p} \frac{y^i_{out,j} - \hat{y}^i_{out,j}}{y^i_{out,j}} \tag{18}$$

Table 7 Statistical evaluation of the best parameter set

Statistics	All points	Training	Validation
χ^2	3.406	2.954	0.452
MSE – CO	5.02×10^{-4}	4.81×10^{-4}	5.87×10^{-4}
MSE – CO_2	4.57×10^{-4}	3.80×10^{-4}	7.64×10^{-4}
MSE – MeOH	8.89×10^{-3}	9.78×10^{-3}	5.33×10^{-3}
MSE – DME	4.34×10^{-3}	4.74×10^{-3}	2.74×10^{-3}
ME – CO	0.0154	0.0149	0.0171
ME – CO_2	0.0144	0.0130	0.0199
ME – MeOH	0.0689	0.0726	0.0541
ME – DME	0.0502	0.0527	0.0404

Results and discussion

Model validation

The group of parameters with the best fit and the respective CI are shown in Table 6, with all eight parameters being statistically significant. The statistical evaluation of the chosen parameter set is shown in Table 7, with a total χ^2 of 3.406 for the best fit and a $CV_{(5)}$ of 3.439. The $CV_{(5)}$ value is close to the best χ^2, which suggests that the model can adequately simulate experiments outside the training set.

The MSE and ME of all optimized species are significantly low, with MeOH and DME showing mean errors of only 7% and 5%, respectively. The MSE and ME values of the training and the validation sets are significantly close, which also points to the good performance of the model outside the training region.

In Fig. 2, parity plots are shown correlating the experiments and simulated results using the best-fit parameter set shown in Table 6.

The simulated concentrations are mostly located inside the ±10% lines of the experimental values, including all H_2 points, all CO points, all CO_2 points, 74% of the MeOH points, and 87% of the DME points. In the parity plot of H_2O, 86% of the points are within ±20% lines. The experiments seem to be affected by H_2O concentrations above 1.5 vol% as a result of condensation effects, most likely due to the pressure-affected analysis stage as well as dead volumes or cold spots. Therefore, condensation of mainly water, but also of MeOH at higher product concentrations may occur. In our study, however, only 12.5% of all points are within this concentration range.

In Fig. 3, experimental and simulated DME and MeOH productivities are shown as a function of CZZ volume fraction (ζ_{CZZ}) for the following operating conditions: CO_2/CO_x inlet ratios of 0.6 (a), 0.75 (b) and 0.9 (c) at 30 bar, 2.78 s^{-1} and 483–513 K in steps of 10 K in between (further CO_2/CO_x inlet ratios are shown in the ESI†).

The dashed lines correspond to the simulated values and the dots correspond to the experimentally measured productivities for MeOH (framed dots) and DME (unframed dots), respectively. The model simulates the trends adequately, with slight underestimations of the DME productivity at 513 K. Here, non-isothermal bed temperature can be excluded from axial temperature measurements with maximum ΔT values of 1.1 K (Fig. S13†).

In Fig. 4, CO and CO_2 conversions are shown, each as a function of ζ_{CZZ} for the following operating conditions: CO_2/CO_x inlet ratios of 0.6 (a), 0.75 (b) and 0.9 (c) at 30 bar, 2.78

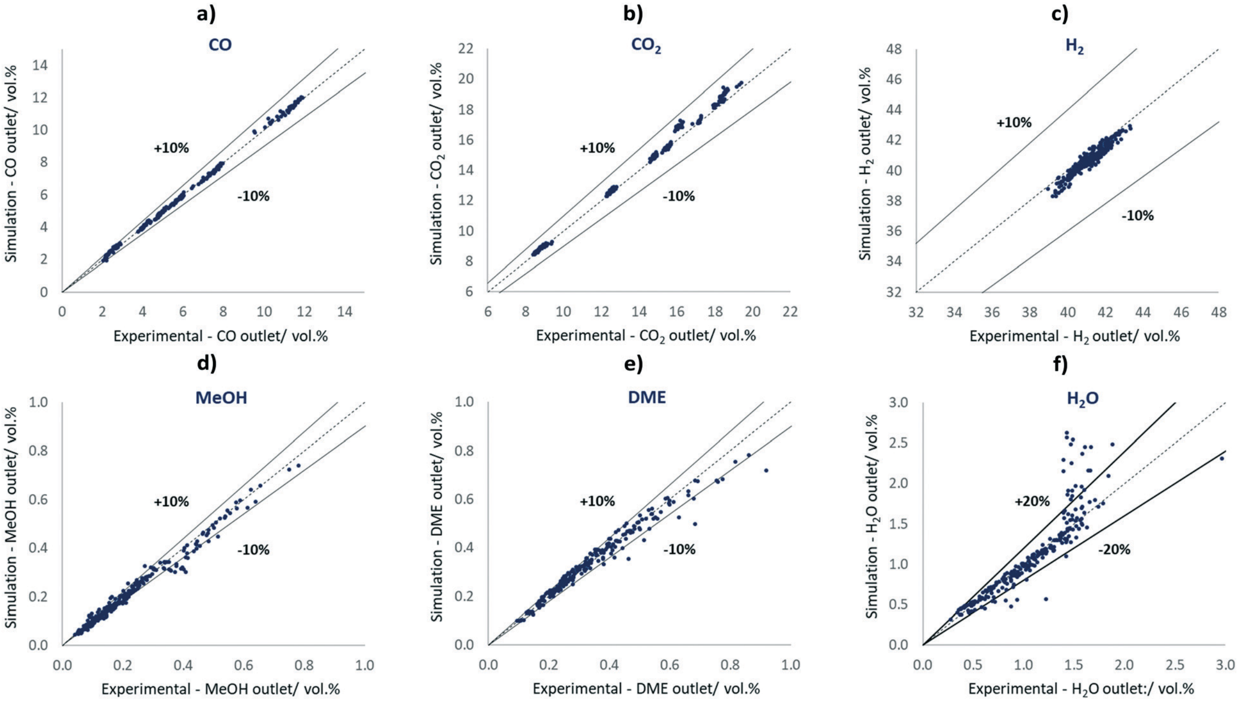

Fig. 2 Parity plots of CO, CO_2, H_2, MeOH, DME and H_2O comparing the 240 simulated results with the respective experimental results.

s^{-1}, and 483–513 K (further CO_2/CO_x inlet ratios are shown in Fig. S7†). The CO and CO_2 conversions are adequately predicted by the kinetic model. At a CO_2/CO_x feed of 0.90, there are some deviations from the experimentally measured CO conversion, probably due to the fact that the initial CO concentration is low, which leads to an amplification of the small deviations in the final CO concentration when calculating the corresponding CO conversion.

DME productivity *vs.* CZZ/FER variation

From the results shown in Fig. 3, it can be observed that an increase in temperature leads to a largely uniform increase in the productivity of DME and MeOH, indicating a strong kinetically controlled operating regime, additionally evidenced by the wide gap from the thermodynamic equilibrium (Fig. S10†). With a ζ_{CZZ} of 0 vol%, no MeOH is formed and the subsequent MeOH dehydration cannot take place and, as a result, no DME is produced. With increasing ζ_{CZZ}, both MeOH and consequently DME are formed. Further increasing ζ_{CZZ} up to *ca.* 90 vol% enhances MeOH and DME productivities, whereby different temperatures or CO_2/CO_x inlet ratios slightly shift the optimum towards more or less CZZ content (see Fig. 7). This indicates that, for ζ_{CZZ} up to *ca.* 90 vol%, FER is in excess, which means that the MeOH dehydration is running close to equilibrium. In this operating region, the rate of the reaction system is controlled only by the MeOH synthesis (over CZZ). A further increase of ζ_{CZZ} leads to a marked decrease in DME productivity and, accordingly, to a sharp increase in non-dehydrated MeOH. This suggests that FER is not in excess anymore, which means that neither the MeOH synthesis nor the MeOH dehydration are in equilibrium, and the rates of the reaction system are determined by both CZZ and FER masses.

High MeOH dehydration activity, as shown here with a FER catalyst component, was similarly reported by Peláez *et al.*[17] with a variation of the CZA/γ-Al_2O_3 catalyst system. In their study, a highest DME yield was achieved with a CO_2-free syngas at a CZA/γ-Al_2O_3 ratio of 92.5 : 7.5 wt%, being close to the experimental CZZ/FER optimum of 95 : 5 wt% reported in this work. In this context, it should be noted that changing the CO_x source from CO to CO_2 increases water production (R3) typically leading to a rapid decrease in dehydration performance when γ-Al_2O_3 is used.[19,21,27,29] In comparison, when the dehydration of MeOH takes place over a solid acid component with fewer Lewis acid sites (known to adsorb water) such as FER,[15,27] HZSM5 (ref. 45–47) or SAPO,[48] high DME productivity can be maintained even at an increased CO_2 content in syngas or in the presence of increased water content. In our study, increasing the CO_2 feed content leads to decreased DME productivity (Fig. 3a–c), being more evident at higher temperatures. Since the thermodynamic influence can be largely ruled out in this operating range (Fig. S10†), it is a kinetically controlled phenomenon. A temperature-controlled decrease in DME and MeOH productivities by increasing the CO_2 content is explained by Sahibzada *et al.*[49] arguing that the lower concentrations of products under differential conditions (low conversion) are less inhibiting MeOH production from CO_2.

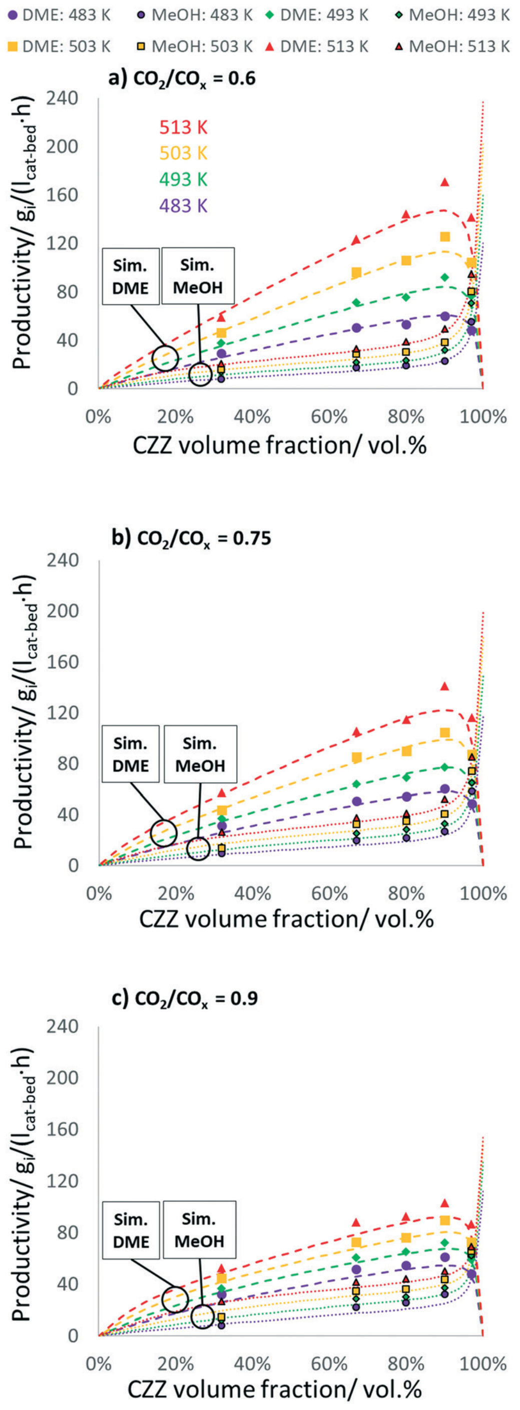

Fig. 3 Comparison of the experimental DME (dots) and MeOH (framed dots) productivities and the simulated values (dashed lines) for a CZZ volume fraction variation at 30 bar, 2.78 s^{-1}, and 483–513 K and the three CO_2/CO_x inlet ratios of 0.6 (a), 0.75 (b) and 0.9 (c) with 20 vol% total CO_x in the feed.

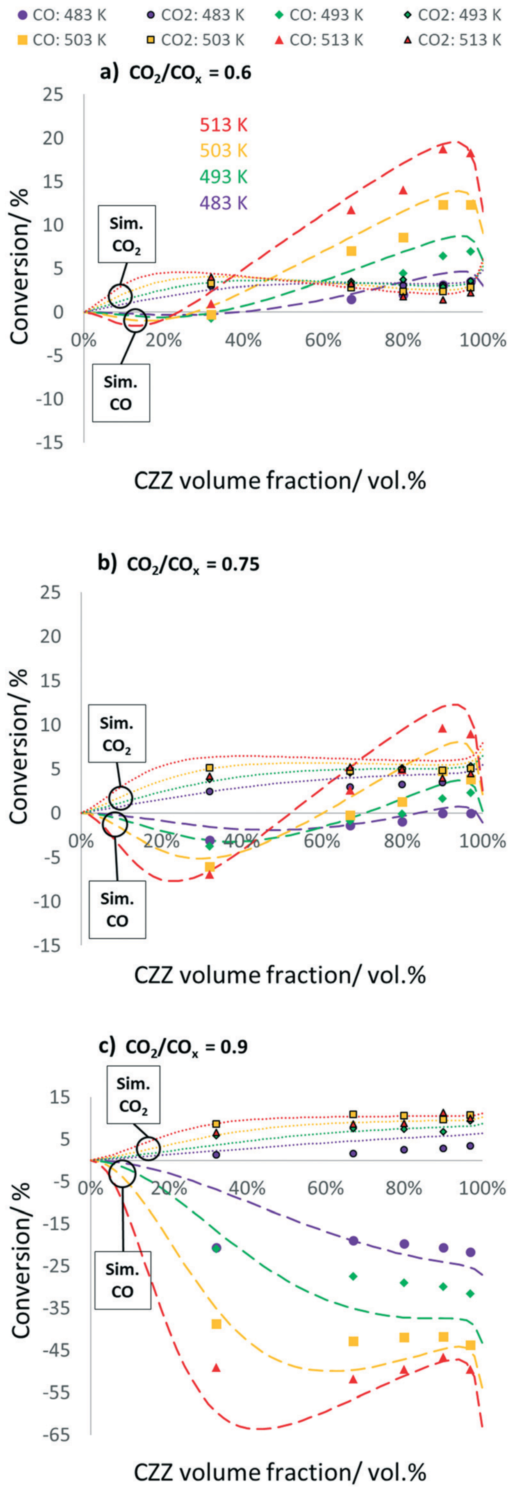

Fig. 4 Comparison of the experimental CO (dots) and CO_2 (framed dots) conversion and the simulated values (dashed lines) for a CZZ volume fraction variation at 30 bar, 2.78 s^{-1}, and 483–513 K and the three CO_2/CO_x inlet ratios of 0.6 (a), 0.75 (b) and 0.9 (c) with 20 vol% total CO_x in the feed.

CO and CO_2 conversion *vs.* CZZ/FER variation

For a CO_2/CO_x inlet ratio of 0.6 (Fig. 4a), an increase in ζ_{CZZ} leads to an increase in CO_2 conversion up to a ζ_{CZZ} of approx. 30 vol%. At ζ_{CZZ} values below 32 vol%, the CO_2 conversion is higher than the CO conversion. Below a ζ_{CZZ} of approx. 23 vol%, CO is produced in small amounts. A further increase of ζ_{CZZ} has a beneficial effect on CO conversion up to a ζ_{CZZ} value of about 95 vol%. Analogously, the CO_2 conversion

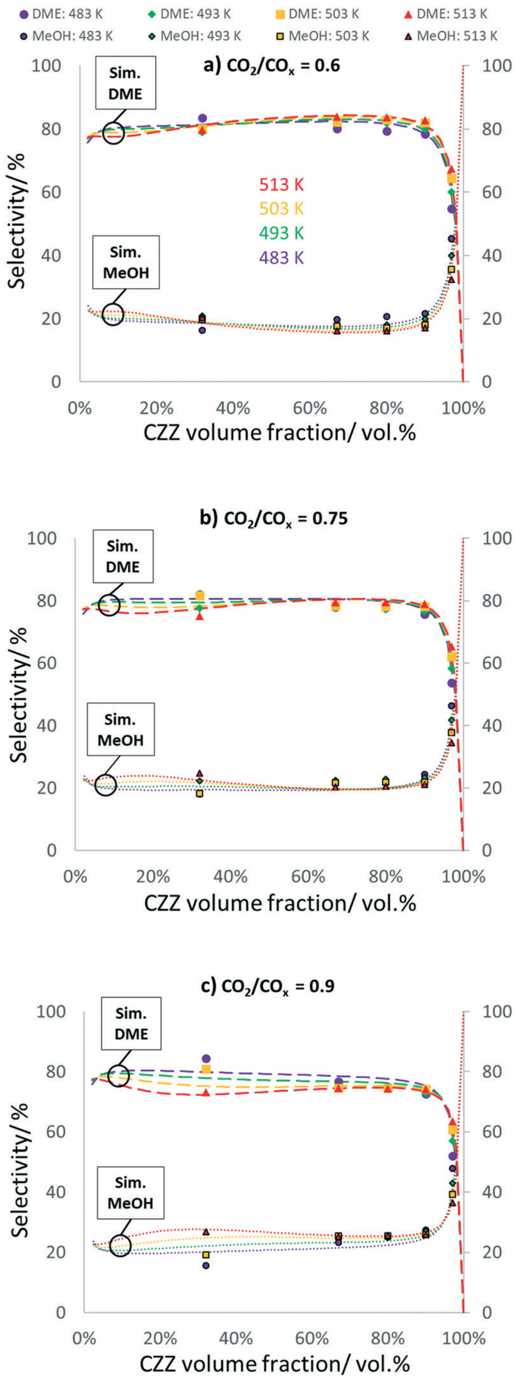

Fig. 5 Comparison of the experimental DME (dots) and MeOH (framed dots) selectivity and the simulated values (dashed lines) for a CZZ volume fraction variation at 30 bar, 2.78 s^{-1}, and 483–513 K and the three CO_2/CO_x inlet ratios of 0.6 (a), 0.75 (b) and 0.9 (c).

decreases slightly. This effect is mainly caused by the fact that the increased MeOH formation leads to increased MeOH dehydration (R4) and thus water formation. The produced water allows higher CO conversion *via* the accelerated WGS reaction (R3) to CO_2 and H_2, partially regenerating the consumed CO_2. At ζ_{CZZ} above approx. 95 vol%, less DME and consequently water are formed, resulting in a reduced WGS reaction rate and thus decreasing CO conversion, leading to a slightly increased CO_2 conversion.

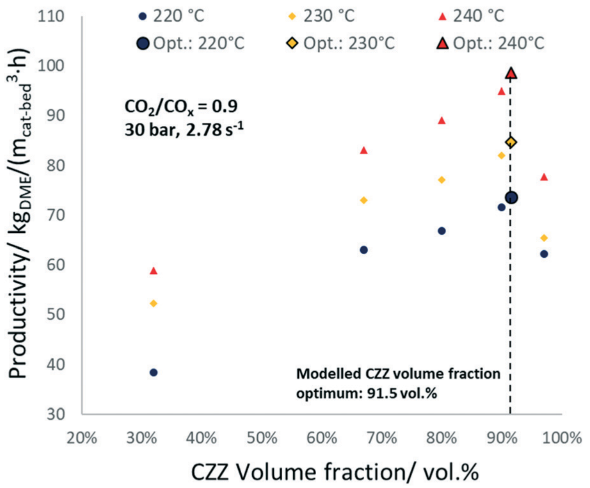

Fig. 6 Comparison of the experimental DME productivity in the run-in period and the model-optimized CZZ/FER volume ratio of 91.5/8.5 at CO_2/CO_x = 0.9, 30 bar, 2.78 s^{-1} and three different temperatures.

An increase in the CO_2/CO_x inlet ratio to 0.75 shows a similar pattern for CO and CO_2 conversion (Fig. 4b) with shifts toward more CO formation at lower ζ_{CZZ} values and less CO conversion at higher ζ_{CZZ} values, these effects being even more pronounced at higher reaction temperatures. At ζ_{CZZ} values above *ca.* 35%, the CO_2 conversion shows almost constant values at the respective measured temperatures, showing that the WGS reaction rate is lowered by less CO in the syngas feed (R3).

Further increasing the CO_2/CO_x inlet ratio to 0.9 (Fig. 4c) leads to a pattern where CO is unexceptionally formed over the entire CZZ/FER variation range *via* the rWGS reaction (R3). The CO_2 conversion is favoured by an increased ζ_{CZZ} value, but to a smaller extent than the CO conversions at lower CO_2/CO_x inlet ratios (Fig. 4a and b). A further potential increase in CO_2 conversion with an optimized CZZ/FER ratio is probably limited by increased water formation from the rWGS reaction occupying the active sites (Cu/Zn) at the CZZ catalyst.[35,36]

In summary, the increase of CO_2 conversion with optimized ζ_{CZZ} is limited due to water formation by CO_2 hydrogenation and MeOH dehydration, accelerating the WGS reaction and preventing the enhancement of CO_2 conversion, whereby this effect being more pronounced at increased temperature. An increase of CO_2 conversion at higher ζ_{CZZ} values should be possible by *in situ* water removal, *e.g.* with a membrane reactor system[50,51] or by doping the CZZ catalyst aiming at stronger binding of formate to the Cu sites, which could inhibit the rWGS reaction and thus accelerate CO_2 hydrogenation on the Cu/Zn sites.[36]

MeOH and DME selectivity *vs.* CZZ/FER variation

In Fig. 5, DME and MeOH selectivities are shown as a function of ζ_{CZZ} for the following operating conditions: CO_2/

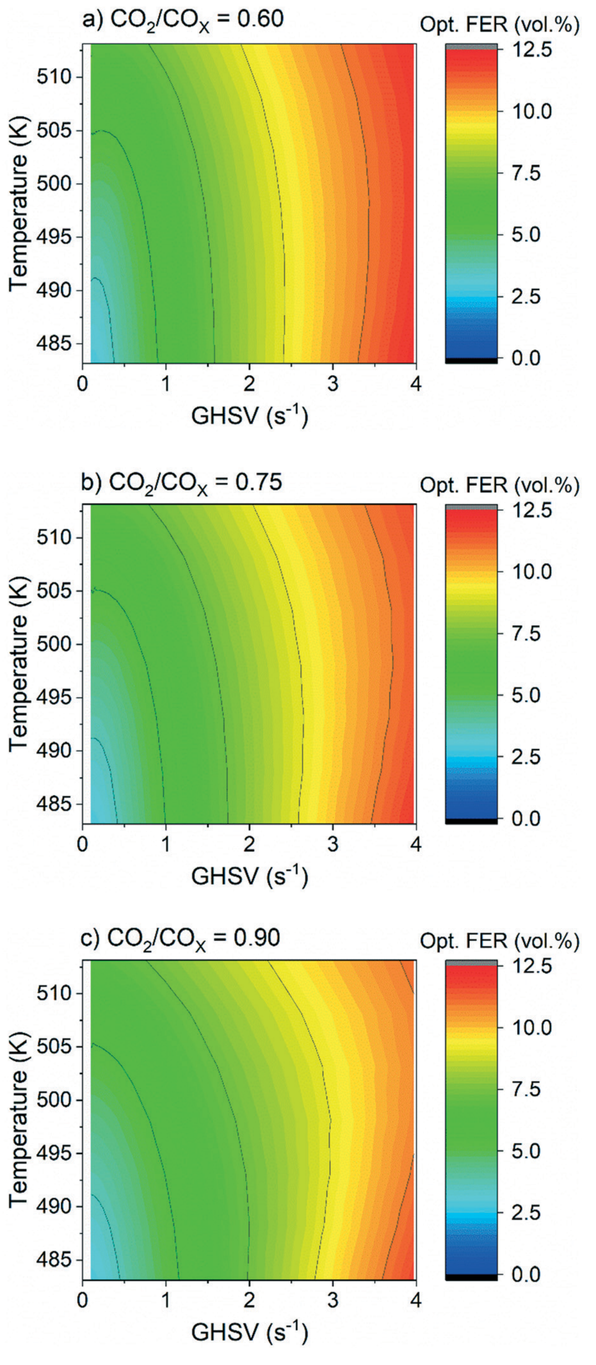

Fig. 7 Contour plots of the optimal FER volume fraction in view of maximum DME productivity under the variation of temperature and GHSV at 30 bar and CO_2/CO_x inlet ratios: 0.6 (a), 0.75 (b) and 0.9 (c).

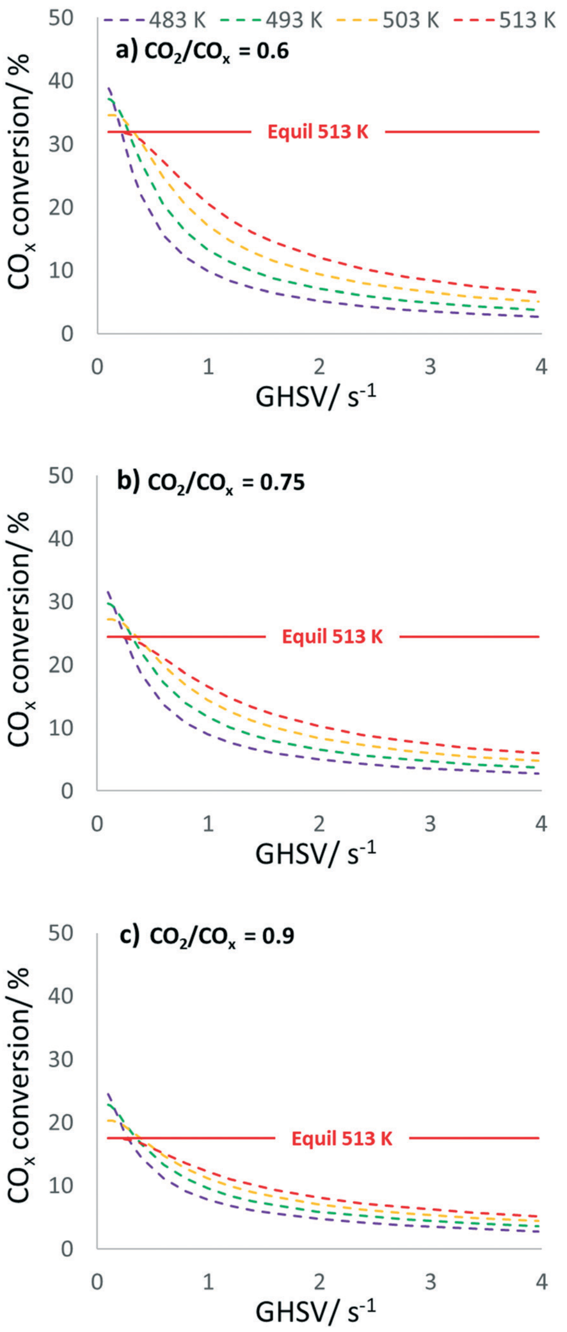

Fig. 8 Simulated CO_x conversion under the variation of GHSV with the optimized CZZ/FER catalyst beds at 30 bar and 483–513 K for the CO_2/CO_x inlet ratios of 0.6 (a), 0.75 (b) and 0.9 (c) and the respective thermodynamic equilibrium at 513 K.

CO_x inlet ratios of 0.6 (a), 0.75 (b) and 0.9 (c) at 30 bar, 2.78 s^{-1}, and 483–513 K, (further CO_2/CO_x inlet ratios are shown in Fig. 8). A similar pattern can be seen for each CO_2/CO_x inlet ratio investigated: high and constant DME selectivities for ζ_{CZZ} up to *ca.* 90 vol% and a sharp decrease of DME when ζ_{CZZ} is increased above 90 vol%.

A higher CO_2 content in the feed slightly decreases DME selectivity, *e.g.* for ζ_{CZZ} = 90 vol%: from 82% (CO_2/CO_x = 0.6) to 75% (CO_2/CO_x = 0.9). The temperature influence on selectivity is not very pronounced. However, for *ca.* $\zeta_{CZZ} < 25$ vol% at CO_2/CO_x = 0.6, for *ca.* $\zeta_{CZZ} < 50$ vol% at CO_2/CO_x = 0.75, and for *ca.* $\zeta_{CZZ} < 90$ vol% at CO_2/CO_x = 0.9, temperature negatively affects DME selectivity. Since for *ca.* $\zeta_{CZZ} < 90$ vol% MeOH dehydration is in equilibrium, the selectivities of MeOH and DME will be affected when this equilibrium is disturbed.

As MeOH dehydration is slightly exothermic (R4), an increase in temperature should directly decrease DME selectivity. Nevertheless, increased temperature is affecting DME selectivity in a more pronounced way by influencing the rWGS reaction (R3) and CO_2 hydrogenation (R2) and thus the water concentration/selectivity (see Fig. S9†). The patterns of the respective water selectivities (eqn (S15)†) clearly display that the changes of DME selectivities follow the inverse trend of the water selectivities.

Optimized CZZ/FER ratio

The validated kinetic model was used to find the optimum FER amount with respect to the highest DME productivity. For a CO_2-rich feed (CO_2/CO_x = 0.9), 30 bar, and 2.78 s^{-1}, an optimal ζ_{CZZ} value of 91.5 vol% was found, with a temperature variation (493–513 K) having only marginal influence under these operating conditions (see Fig. 7c). This simulated optimum ζ_{CZZ} value was experimentally validated, following the same run-in period as the catalyst beds in Table 2. Fig. 6 shows the DME productivities of the run-in period (unframed dots) and the experimental validation of the model-based optimized catalyst bed (framed dots).

Compared to the catalyst bed with the highest experimental DME productivity (ζ_{CZZ} = 90 vol%), the simulated optimal value (ζ_{CZZ} = 91.5 vol%) achieved a slight relative increase in DME productivity at all measured temperatures: 493 K (2.9%), 503 K (3.2%), and 513 K (3.8%). Since the present model adequately simulated the experiments, it is applied to investigate the optimum FER volume fraction (ζ_{FER}) within a broader GHSV range, including industrially relevant operating conditions. In Fig. 7, the optimized FER amounts are shown at 30 bar and CO_2/CO_x inlet ratios of 0.6 (a), 0.75 (b) and 0.9 (c) and under a variation of temperature and GHSV. The FER optimum value is mostly affected by the GHSV, with less FER being necessary for lower GHSV (achieving ζ_{FER} values lower than 5 vol%). Increasing the temperature slightly increases the FER optimum amount, while increasing the CO_2 content in the feed marginally decreases the FER optimum amount. Since lower GHSV leads to increased CO_x conversion and thus enhanced DME production, higher water accumulation is expected. The lower FER amount required for an optimized DME productivity at lower GHSV is therefore a hint that the activity of FER is less affected by water accumulation than the activity of CZZ. This hypothesis is supported by the fact that the optimum FER amount is slightly lower for higher CO_2/CO_x inlet ratios (*cf.* Fig. 7a–c), which also increase water formation.

In Fig. 8, CO_x conversion is plotted against the GHSV under the same conditions considered in Fig. 7. The GHSV variation shows a clearly kinetically dominated range between 1 and 4 s^{-1}, while an increase in the thermodynamic control is expected as GHSV decreases, with CO_x conversion achieving its equilibrium at 513 K.

By using process parameters of 513 K and a CO_2/CO_x inlet ratio of 0.6, a GHSV of 0.4 s^{-1} leads to 95.8% of the thermodynamically possible CO_x conversion ($X_{CO_x,equil}$ = 31.9%) at a DME selectivity of 90.1%, while CO_2/CO_x = 0.75 affords 95.4% of the possible conversion ($X_{CO_x,equil}$ = 24.4%) at a DME selectivity of 87.4%, and CO_2/CO_x = 0.9 affords 94.8% of the possible conversion ($X_{CO_x,equil}$ = 17.6%) at a DME selectivity of 83.4%. A GHSV of 0.4 s^{-1} corresponds to a seven times lower volume flow, chosen in the kinetic measurements presented here. Further simulations were performed at 60 bar and without N_2 dilution ($H_2/CO/CO_2$ in the feed = 70/12/18 vol%), *i.e.* closer to industrial conditions. Although this requires a greater extrapolation of our model, the preliminary and interesting finding is that in this case probably even lower amounts of FER (less than 3 vol%) already ensure efficient DME production. From simulation at 513 K, such an optimized CZZ/FER bed ratio enables a CO_x conversion of more than 47% at a GHSV below 0.4 s^{-1} (Fig. S11 and S12†), which corresponds to 90.3% of the thermodynamically possible CO_x conversion ($X_{CO_x,equil}$ = 52.2%) at a DME selectivity of 88.9%. Further experimental validation in this operating range would be valuable to back up these promising simulated results.

Other CZZ catalysts with different properties (*cf.* Table 4) as well as ferrierites (*cf.* Table 5) with other Si/Al ratios would require a refit of the parameter set (Table 6) and possibly a new evaluation of the result interpretation.

Conclusions

Kinetic experiments for direct DME synthesis were carried out under various operating conditions, with particular emphasis on the CZZ/FER bed composition. A new kinetic model was developed and validated with a vast array of experimental data. It was applied in model-based optimization to determine the optimal FER volume fraction with respect to DME productivity under the variation of temperature, GHSV and CO_2/CO_x inlet ratios. An optimum CZZ/FER catalyst bed ratio (91.5/8.5 vol%) for a CO_2-rich feed was calculated with the model and then validated experimentally verifying that the results obtained from the optimization are accurate. Extrapolations of the model to process conditions closer to industrially relevant conditions showed that the optimal FER volume fraction actually decreases at lower GHSV. From these findings, the necessity for additional validation beyond the scope of the present study is derived, which is the subject of current investigations. Our experiments, together with the results from modelling also underline that water formation from MeOH dehydration accelerates the WGS reaction regenerating CO_2. This at first prevents a significant increase of CO_2 conversion with an optimized catalyst bed, which is why alternative reactor concepts where water can be separated *in situ*, *e.g.* membrane reactors, appear promising. In the outlook for a further possibility to increase CO_2 conversion, a catalyst modification (*e.g.*, with promoters) could be purposeful, which strengthens binding of the intermediate formate to the Cu sites, which otherwise inhibit the rWGS reaction and thus accelerate CO_2 hydrogenation over Cu/Zn. We believe that the model presented here is particularly well suited to describe and predict the reaction kinetics and to support the search for an optimal reactor and/or process design for direct DME synthesis due to its broad range of validity.

Conflicts of interest

There are no conflicts to declare.

Acknowledgements

We acknowledge the Helmholtz Association for funding this research (Research Programme "Storage and Cross-linked Infrastructures", Topic "Synthetic Hydrocarbons"). We thank the Coordenação de Aperfeiçoamento de Pessoal de Nível Superior (CAPES) for financing the PhD scholarship of Bruno Lacerda de Oliveira Campos (Process Number: 88881.174609/2018-01). We kindly acknowledge the support of TVT-KIT group, analytics and chemical laboratory colleagues and especially Sabrina Polierer and Lucas Warmuth from IKFT-KIT for their support in characterization.

References

1 N. Dahmen, U. Arnold, N. Djordjevic, T. Henrich, T. Kolb, H. Leibold and J. Sauer, *J. Supercrit. Fluids*, 2015, **96**, 124–132.
2 A. Varone and M. Ferrari, *Renewable Sustainable Energy Rev.*, 2015, **45**, 207–218.
3 A. Buttler and H. Spliethoff, *Renewable Sustainable Energy Rev.*, 2018, **82**, 2440–2454.
4 G. A. Olah, A. Goeppert and G. S. Prakash, *J. Org. Chem.*, 2009, **74**, 487–498.
5 E. Catizzone, G. Bonura, M. Migliori, F. Frusteri and G. Giordano, *Molecules*, 2018, **23**, 1–31.
6 B. V. Ga and P. Q. Thai, *Appl. Sci.*, 2020, **10**, 3416–3434.
7 M. R. Gogate, *Pet. Sci. Technol.*, 2018, **36**, 562–568.
8 Z. Azizi, M. Rezaeimanesh, T. Tohidian and M. R. Rahimpour, *Chem. Eng. Process.*, 2014, **82**, 150–172.
9 V. Dieterich, A. Buttler, A. Hanel, H. Spliethoff and S. Fendt, *Energy Environ. Sci.*, 2020, **13**, 3207–3252.
10 S. Ahlgren, A. Baky, S. Bernesson, Å. Nordberg, O. Norén and P. A. Hansson, *Biosyst. Eng.*, 2008, **99**, 145–155.
11 J. Ereña, I. Sierra, A. T. Aguayo, A. Ateka, M. Olazar and J. Bilbao, *Chem. Eng. J.*, 2011, **174**, 660–667.
12 Y. Wang, H. Liu, H. Zhang and W. Ying, *React. Kinet., Mech. Catal.*, 2016, **119**, 585–594.
13 S. M. K. Aboul-Fotouh, L. I. Ali, M. A. Naghmash and N. A. K. Aboul-Gheit, *J. Fuel Chem. Technol.*, 2017, **45**, 581–588.
14 M. Sánchez-Contador, A. Ateka, P. Rodriguez-Vega, J. Bilbao and A. T. Aguayo, *Ind. Eng. Chem. Res.*, 2018, **57**, 1169–1178.
15 F. Frusteri, M. Migliori, C. Cannilla, L. Frusteri, E. Catizzone, A. Aloise, G. Giordano and G. Bonura, *J. CO2 Util.*, 2017, **18**, 353–361.
16 R. Ahmad, D. Schrempp, S. Behrens, J. Sauer, M. Döring and U. Arnold, *Fuel Process. Technol.*, 2014, **121**, 38–46.
17 R. Peláez, P. Marín and S. Ordóñez, *Fuel Process. Technol.*, 2017, **168**, 40–49.
18 J. Guang-xin, M. Hong-bin, T. Yi-sheng and H. Yi-zhuo, *Ind. Eng. Chem. Res.*, 2005, **44**, 2011–2015.
19 C. Peinado, D. Liuzzi, M. Retuerto, J. Boon, M. A. Peña and S. Rojas, *Chemical Engineering Journal Advances*, 2020, **4**, 100039–100047.
20 J.-W. Bae, H. S. Potdar, S.-H. Kang and K.-W. Jun, *Energy Fuels*, 2008, **22**, 223–230.
21 N. Delgado Otalvaro, G. Sogne, K. Herrera Delgado, S. Wild, S. Pitter and J. Sauer, *RSC Adv.*, 2021, **11**, 24556–24569.
22 J. Abu-Dahrieh, D. Rooney, A. Goguet and Y. Saih, *Chem. Eng. J.*, 2012, **203**, 201–211.
23 A. García-Trenco, A. Vidal-Moya and A. Martínez, *Catal. Today*, 2012, **179**, 43–51.
24 S. Ren, S. Li, N. Klinghoffer, M. Yu and X. Liang, *Carbon Resour. Convers.*, 2019, **2**, 85–94.
25 G. Jia, Y. Tan and Y. Han, *Ind. Eng. Chem. Res.*, 2006, **45**, 1152–1159.
26 F. Arena, K. Barbera, G. Italiano, G. Bonura, L. Spadaro and F. Frusteri, *J. Catal.*, 2007, **249**, 185–194.
27 S. Wild, S. Polierer, T. A. Zevaco, D. Guse, M. Kind, S. Pitter, K. Herrera Delgado and J. Sauer, *RSC Adv.*, 2021, **11**, 2556–2564.
28 S. Polierer, D. Guse, S. Wild, K. Herrera Delgado, T. N. Otto, T. A. Zevaco, M. Kind, J. Sauer, F. Studt and S. Pitter, *Catalysts*, 2020, **10**, 816–833.
29 E. Catizzone, M. Migliori, A. Purita and G. Giordano, *J. Energy Chem.*, 2019, **30**, 162–169.
30 B. Voss, A. Katerinopoulou, R. Montesano and J. Sehested, *Chem. Eng. J.*, 2019, **377**, 121940.
31 S. Guffanti, C. G. Visconti and G. Groppi, *Ind. Eng. Chem. Res.*, 2020, **59**, 14252–14266.
32 G. Fierro, G. Ferraris and G. Moretti, *Appl. Catal., B*, 2009, **91**, 499–506.
33 Y. T. Kim, K.-D. Jung and E. D. Park, *Microporous Mesoporous Mater.*, 2010, **131**, 28–36.
34 B. Lacerda de Oliveira Campos, K. Herrera Delgado, S. Pitter and J. R. Sauer, *Ind. Eng. Chem. Res.*, 2021, **60**, 15074–15086.
35 F. Studt, M. Behrens, E. L. Kunkes, N. Thomas, S. Zander, A. Tarasov, J. Schumann, E. Frei, J. B. Varley, F. Abild-Pedersen, J. K. Nørskov and R. Schlögl, *ChemCatChem*, 2015, **7**, 1105–1111.
36 B. Lacerda de Oliveira Campos, K. Herrera Delgado, S. Wild, F. Studt, S. Pitter and J. Sauer, *React. Chem. Eng.*, 2021, **6**, 868–887.
37 J. D. Grunwaldt, A. M. Molenbroek, N. Y. Topsøe, H. Topsøe and B. S. Clausen, *J. Catal.*, 2000, **194**, 452–460.
38 S. Kuld, M. Thorhauge, H. Falsig, C. F. Elkjær, S. Helveg, I. Chorkendorff and J. Sehested, *Science*, 2016, **352**, 969–974.
39 C. Ovesen, B. Clausen, J. Schiøtz, P. Stoltze, H. Topsøe and J. K. Nørskov, *J. Catal.*, 1997, **168**, 133–142.
40 L. Meng and Y.-Y. Duan, *Fluid Phase Equilib.*, 2005, **238**, 229–238.
41 L. Meng, Y.-Y. Duan and X.-D. Wang, *Fluid Phase Equilib.*, 2007, **260**, 354–358.

42 A. A. Arvidsson, P. N. Plessow, F. Studt and A. Hellman, *J. Phys. Chem. C*, 2020, **124**, 14658–14663.

43 J. Gareth, W. Daniela, H. Trevor and T. Robert, *An introduction to statistical learning: with applications in R*, Spinger, 2013.

44 Y. Slotboom, M. J. Bos, J. Pieper, V. Vrieswijk, B. Likozar, S. R. A. Kersten and D. W. F. Brilman, *Chem. Eng. J.*, 2020, **389**, 124181–124196.

45 G. Bonura, M. Cordaro, L. Spadaro, C. Cannilla, F. Arena and F. Frusteri, *Appl. Catal., B*, 2013, **140–141**, 16–24.

46 J. Ereña, R. Garoña, J. M. Arandes, A. T. Aguayo and J. Bilbao, *Catal. Today*, 2005, **107–108**, 467–473.

47 Y. Zhang, Y. Zhang, F. Ding, K. Wang, W. Xiaolei, B. Ren and J. Wu, *Chem. Ind. Chem. Eng. Q.*, 2017, **23**, 49–56.

48 A. Ateka, J. Ereña, P. Pérez-Uriarte, A. T. Aguayo and J. Bilbao, *Int. J. Hydrogen Energy*, 2017, **42**, 27130–27138.

49 M. Sahibzada, I. S. Metcalfe and D. Chadwick, *J. Catal.*, 1998, **174**, 111–118.

50 N. Diban, A. M. Urtiaga, I. Ortiz, J. Ereña, J. Bilbao and A. T. Aguayo, *Chem. Eng. J.*, 2013, **234**, 140–148.

51 S. Poto, F. Gallucci and M. Fernanda Neira d'Angelo, *Fuel*, 2021, **302**, 121080–121093.